NANO LETTERS
Cite This: Nano Lett. 2019, 19, 512−519
Letter
pubs.acs.org/NanoLett

Lithiation-Aided Conversion of End-of-Life Lithium-Ion Battery Anodes to High-Quality Graphene and Graphene Oxide

Yunya Zhang,[#] Ningning Song,[#] Jiajun He, Ruoxi Chen, and Xiaodong Li*

Department of Mechanical and Aerospace Engineering, University of Virginia, 122 Engineer's Way, Charlottesville, Virginia 22904-4746, United States

Supporting Information

ABSTRACT: In the past two decades, lithium-ion (Li-ion) batteries have transformed the appearance of the world. Along with the ever-increasing production and usage are the tremendous number of retired batteries, which have created social and environmental issues, making battery recycling an urgent task. Graphene has exhibited outstanding electronic and mechanical properties but it is still difficult to fabricate high-quality graphene with feasible procedures at low cost. Here, a strategy of smartly converting retired Li-ion battery anodes to graphene and graphene oxide is proposed. The graphite powders collected from end-of-life Li-ion batteries exhibited irregular expansion because of the lithium-ion intercalation and deintercalation in the anodegraphite during battery charge/discharge. Such prefabrication process facilitated both chemical and physical exfoliations of the graphite. Comparing with the graphene oxide derived from pristine, untreated graphite, the graphene oxide from anodegraphite exhibited superlative homogeneity and electrochemical properties. The lithiation aided pre-expansion enabled 4 times enhancement of graphene productivity by shear mixing. Furthermore, the graphene fabrication was seamlessly inserted into the currently used battery recycling streamline in which the acid treatment was found to further swell the graphite lattice, pushing up the graphene productivity to 83.7% (10 times higher than that of pristine graphite powders). The findings create new opportunities for capitalizing on waste batteries to produce high-quality graphene and its derivatives.

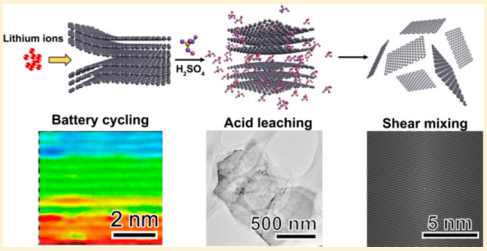

KEYWORDS: *Lithium-ion battery, graphene, graphene oxide, recycle, shear mixing*

The lithium-ion (Li-ion) battery has been employed as the major energy storage system and has had a huge impact on human society in the past two decades due to its high-energy density, long lifespan, and outstanding stability.[1−5] Considering the ever-increasing electric vehicle (EV) market, the Li-ion battery industry has the potential of continuing its fast expansion.[6] It is estimated that global Li-ion battery sales will reach $221 billion annually in the year of 2024.[7−9] However, accompanying the booming expansion of the Li-ion battery market, a tremendous amount of batteries retire every year and most of them are disposed of in landfills, which not only causes severe waste of precious sources[10−12] but also induces hazardous soil contamination due to the plastic components and toxic electrolytes.[13] So far, only 1% of end-of-life Li-ion batteries have been recycled.[14] Apparently, it is an urgent necessity to develop effective battery recycling techniques. Several strategies about recycling metallic parts, such as Cu, Fe, Al, and cathode materials from end-of-life Li-ion batteries have been designed.[15−23] Smelting, thermal treatment, and acid leaching processes were employed in battery recycling.[18−23] Wang et al.[17] designed an acid leaching process to derive $LiCo_xNi_yMn_zO_2$ salts from cathodes, which has the potential to be scaled up for industrial production. However, acid leaching techniques focus on cathode materials alone while largely overlooking the anodes in battery recycling. Can we take advantage of the acid leaching method to simultaneously recycle all battery components?

Graphene, a single layer of carbon atoms, is known for its outstanding mechanical and electronic properties,[24−27] making graphene a promising material for numerous applications, especially for future industrial development.[28−31] Since the initial discovery, multiple methods have been developed to produce graphene. Chemical vapor deposition (CVD) can produce large, intact graphene.[32−34] However, the graphene synthesized by the CVD method, which is expensive and inefficient, is difficult to separate from the substrate for further applications. An alternative is to fabricate graphene oxide by exfoliating graphite via strong oxidation agents (Hummers method).[35] The graphene oxide sheets are often attached by various functional groups, resulting in several unique properties.[36] However, this process will inevitably lead to a destruction of crystal structure, largely deteriorating the mechanical properties of graphene. Moreover, the consumption of strong oxidants and the complicated procedures increase the cost, which has hindered the scale-up for industrial production.[37,38] The shear mixing method was recently developed, which largely improved the productivity and

Received: November 1, 2018
Revised: December 4, 2018
Published: December 19, 2018

DOI: 10.1021/acs.nanolett.8b04410
Nano Lett. 2019, 19, 512−519

efficiency of graphene fabrication. However, the overall productivity still cannot meet the requirements of industrial production and the obtained graphene sheets must be stored in organic solvents or alkane to inhibit aggregation.[39−42] Prior to all the technical difficulties, the raw material, graphite, is a nonrenewable resource while the mining of graphite causes severe environmental pollution, leaving irreversible damage to the landscape. A rational strategy to simultaneously solve the environmental issues from waste batteries and graphite mining is to fabricate graphene directly from end-of-life battery anodes. Unlike cathode materials, recycling of graphite anode has received little attention. Previously, the recycling of the anode mainly focused on the metal parts.[43] Graphite powders were then reactivated via heat and chemical treatments and reused for constructing new Li-ion batteries.[44,45] Recently, researchers attempted to extract lithium from the graphite anode.[46] Although these studies have made huge progress on anode recycling, new techniques that efficiently produce high-value-added products from battery anodes are needed.[47] How did battery cycling influence the anode graphite? Can we utilize the battery charge/discharge process to facilitate the conversion of battery anode graphite into graphene?

Here, graphite powders from end-of-life Li-ion battery anodes were used to fabricate graphene (Scheme 1). High-resolution transmission electron microscopy (HRTEM) inspection (Figure 1) revealed that the lattice of anode graphite powders was expanded irregularly. Molecular dynamic (MD) simulations (Figure 2) uncovered that the lattice expansion originated from the lithium-ion intercalation and deintercalation during battery charge and discharge. Such lattice expansion of graphite can be considered as a prefabrication of graphene because it weakened the van der Waals bonds and facilitated the exfoliation. A simplified Hummers method was first employed to fabricate graphene oxide from anode graphite powders. The as-obtained graphene oxide exhibited superlative homogeneity and excellent electrochemical performance. Shear mixing was then used to produce graphene. Comparing with the productivity of the graphene derived from pristine graphite powders purchased from Sigma-Aldrich, the graphene productivity was improved 4 times by simply using anode graphite. To achieve a complete battery recycling, we need to insert the proposed strategy seamlessly into the existing cathode material recycling processes. The H_2SO_4 treatment further enlarged the graphite lattice, enabling a largely enhanced graphene productivity of 83.7% (10 times higher than that of pristine graphite powders). The produced graphene sheets retained intact crystal structure and could remarkably reinforce epoxy. The proposed design provides a new wisdom of recycling retired Li-ion batteries and has the potential to accelerate the development of graphene and derived products.

Scheme 1. Schematic Illustration of the Proposed Smart Fabrication of Graphene and Graphene Oxide from End-of-Life Batteries[a]

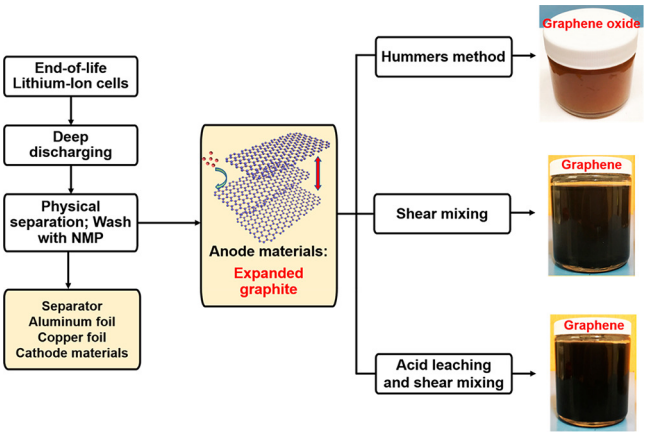

[a]End-of-life Li-ion batteries were collected from personal electronic devices. The retired batteries were deeply discharged before being dismantled. The expanded graphite powders were obtained from the anodes and were then converted into high-quality graphene and graphene oxide.

Swelled Graphite from End-of-Life Li-Ion Batteries. An end-of-life battery with the capacity of 900 mAh (Figure 1a) was deeply discharged to 0 V before being dismantled. The anode, cathode, and separator were carefully separated without severe damage (Figure 1b). The anode comprised graphite powders, binder (PVDF), and a copper film as the current collector. X-ray diffraction (XRD) inspection revealed a typical graphite pattern (Figure 1c). Unlike the XRD spectrum, the X-ray photoelectron spectroscopy (XPS) spectrum of untreated anode graphite exhibited a high concentration of O, F, Li, and P (Figure S1a in Supporting Information), indicating that an amorphous solid-electrolyte-interphase (SEI) layer had formed on the graphite surface. To eliminate the impurity, the anode was washed with *N*-methyl-2-pyrrolidone (NMP), ethanol, and diluted water. The cleaned anode graphite only had C and O peaks in the XPS spectrum (Figure S1b), indicating that SEI was completely removed. Scanning electron microscopy (SEM) observation demonstrated that the cleaned graphite powders were particles (Figure 1d) of 6−30 μm in size (the majority of particles were in the range 10−20 μm (Figure S2)). Close-up high-resolution transmission electron microscopy (HRTEM) inspection revealed that the lattice of the electrochemically cycled graphite was enlarged along the crystallographic *c*-direction (Figure S3a). The average interplanar spacing was determined to be 0.352 nm, corresponding to 3.5% lattice expansion. Some graphite lattices swelled up to 0.39 nm, equal to a 14.7% lattice expansion (Figure S3b). To further uncover such lattice expansion, the deformation field obtained from digital image correlation (DIC) analysis along the crystallographic *c*-direction (Figure 1f) was obtained by processing the HRTEM image (Figure 1e) with reference to a perfect graphite crystal lattice ($P6_3\,mc$ space group, $a = b = 2.47$ Å and $c = 6.79$ Å[48]), showing wave-like inhomogeneous lattice expansion. The interplanar spacing dilation of graphite has been previously identified as a consequence of lithium-ion intercalations.[49,50] A reasonable assumption is that the repeated insertion of lithium ions into graphite layers weakened the van der Waals bonds between the graphene layers, leading to the change in interplanar spacing.

Molecular dynamic (MD) calculations were carried out to atomistically quantify the lattice expansion of graphite during lithiation/delithiation (Figure 2a). The stoichiometry of lithium-graphite intercalation compounds (Li_xC_6, x ranges from 0 to 1) and the related structural features have been well studied.[51,52] Here, the lithium-ion intercalated graphite compound LiC_{12} (Figure S4) was selected to represent the product of the Li-ion battery during the charging process. To reveal the evolution of the interplanar spacings along the crystallographic *c*-direction of graphite during battery cycling,

DOI: 10.1021/acs.nanolett.8b04410
Nano Lett. 2019, 19, 512−519

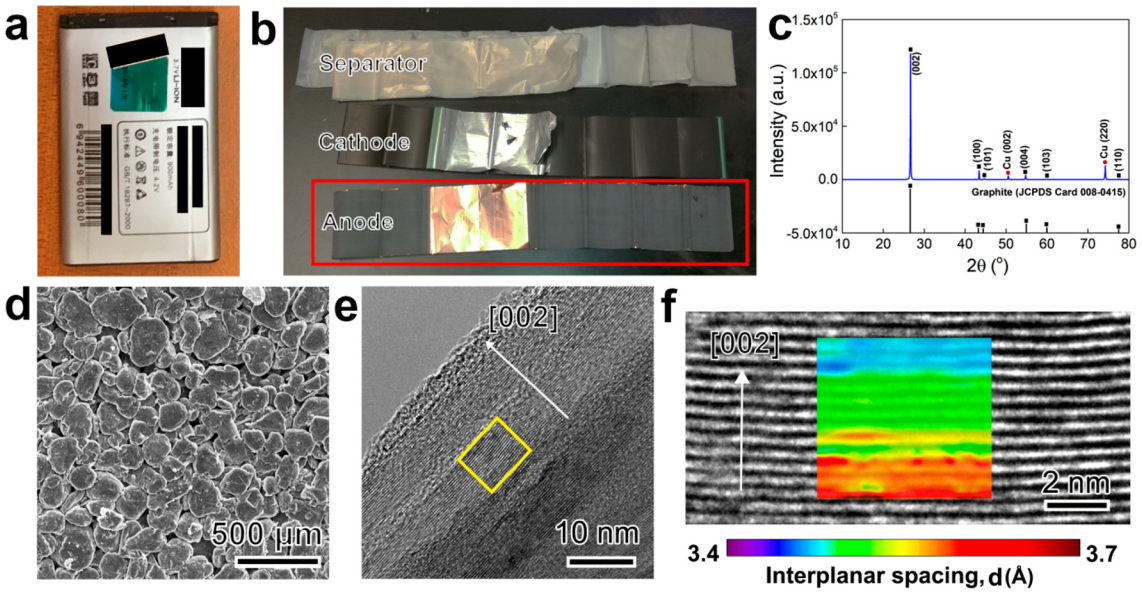

Figure 1. Swelled graphite from end-of-life Li-ion batteries. (a) An end-of-life battery. (b) Separator, cathode, and anode of the battery after manually dismantling. (c) XRD pattern of the anode. (d) SEM image of the anode graphite powders. (e) HRTEM inspection of the graphite powders. (f) Lattice expansion in the graphite revealed by DIC.

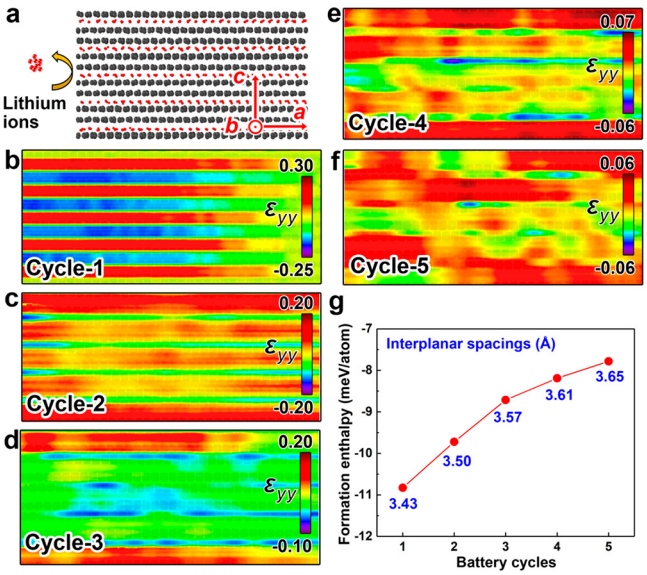

Figure 2. MD simulations of the lithiation/delithiation process in graphite during battery charge/discharge. (a) Side view of the atomic structure of lithium-ion intercalated graphite compound (LiC_{12}). (b)−(f) Lattice strain fields after each lithiation/delithiation cycle by coupling MD simulations and DIC. (g) Formation enthalpy of bilayer graphite with various interlayer spacings at 0 K calculated by first principles.

the lithiation/delithiation process was performed for five cycles. The obtained snapshots of atomic configurations after each cycle were processed with reference to the ones at the beginning of this cycle via DIC (Figure 2b−f). During the first cycle, the atomic strain field (ε_{yy}, along the *c*-direction) revealed that the lattice was partially expanded and partially compressed. In the following lithiation/delithiation cycles, the atomic strain distributions gradually become nonuniform, consistent with the experimental observations (Figure 1f). The average interplanar spacings of graphite after each cycle were calculated to be 3.43, 3.50, 3.57, 3.61, and 3.65 Å, respectively. After five cycles of lithiation/delithiation, the total volume of the simulated graphite crystal increased by 7.35%. During the charging process, the kinetic energy of lithium ions is progressively converted into the strain energy of graphite, leading to lattice expansion, which cannot be completely recovered after battery discharging.

Density functional theory (DFT) calculations were performed to obtain the formation enthalpy (ΔH(bilayer), meV/atom) of bilayer graphite at 0 K (Figure S5), which is defined as

$$\Delta H(\text{bilayer}) = [H(\text{bilayer}) - 2H(\text{monolayer})]/n$$

where n is the total number of atoms. On the basis of the MD simulations, the unit formation enthalpies were calculated as a function of the interplanar spacings of graphite (Figure 2g). The negative formation energies presented the high stability of the graphite. As the lattice spacings increased, the formation enthalpies also increased, which is consistent with previous work.[53] Therefore, the volume expansion can reduce the binding energy of graphite, that is, weakening the bonding strength, which is expected to facilitate both chemical and mechanical exfoliation processes. Armed with the experimental observations and theoretical calculations, it is concluded that battery cycling can be considered as a prefabrication of graphene.

Fabrication of Graphene Oxide from Anode Graphite. Graphene oxide, which was also called graphitic acid, is highly defective, containing a large amount of chemical (functional groups) and structural (vacancies and voids) defects.[54] The functional groups and defects, although they deteriorate the conductivity and mechanical properties of graphene, give graphene oxide several unique properties, such as hydrophilicity, dispersity, and absorbability, endowing graphene oxide with wide applications in various fields. Currently, graphene oxide is often fabricated by Hummers method,[35−38] which requires expanding graphite at low temperature and then exfoliating graphene at relatively high temperature. The multistaged procedure is time and energy consuming. Since

DOI: 10.1021/acs.nanolett.8b04410
Nano Lett. 2019, 19, 512−519

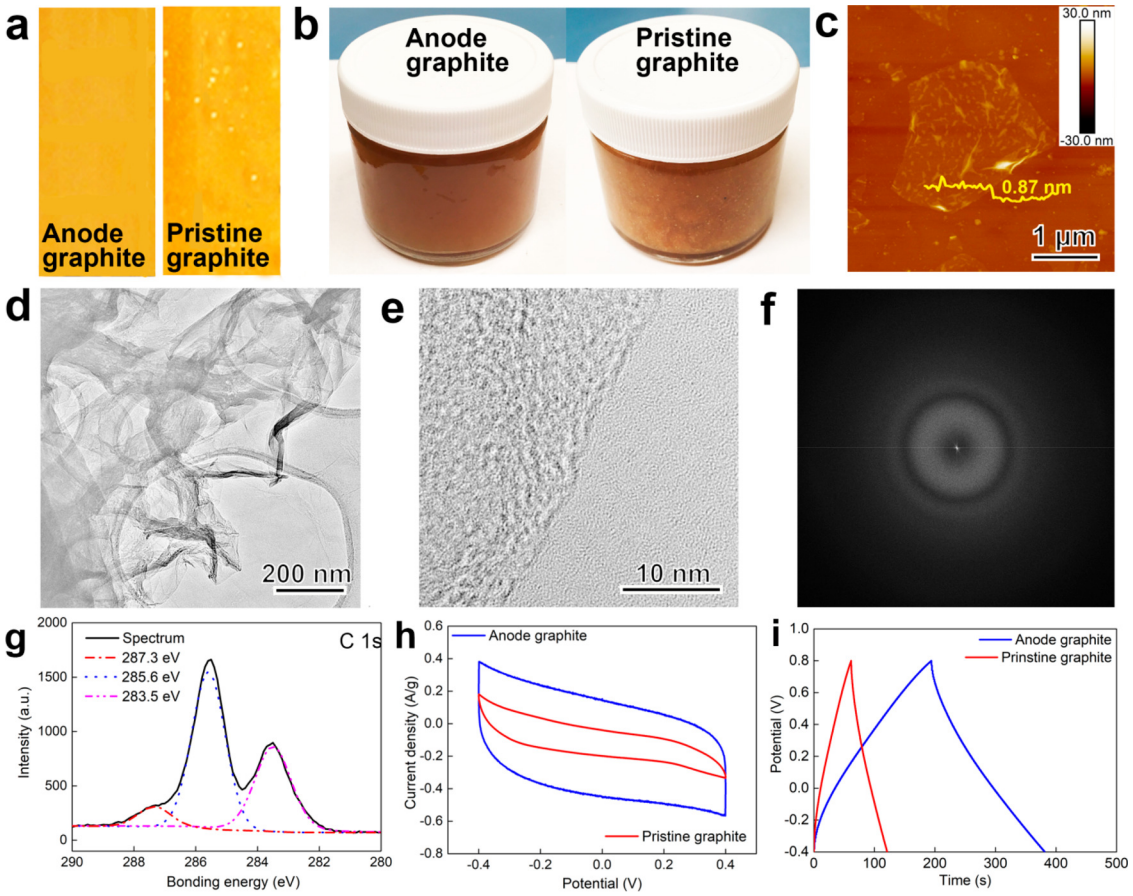

Figure 3. Graphene oxide derived from end-of-life battery anodes. (a) Digital photos of as-fabricated graphene oxide from anode graphite and pristine graphite. (b) Digital photos of graphene oxide from anode graphite and pristine graphite after centrifuging and diluting. (c) AFM height profile of the as-fabricated graphene oxide flakes from anode graphite. (d) TEM inspection of the graphene oxide flakes from anode graphite. (e) HRTEM image of the graphene oxide flakes from anode graphite, showing no crystal structure. (f) FFT of Figure 3e. (g) XPS spectrum of C 1s peak. (h) Comparative CV curves of symmetric supercapacitors assembled separately with reduced graphene oxide derived from anode graphite and pristine graphite. (i) Comparative galvanostatic curves of the assembled symmetric supercapacitors.

the anode graphite was preswelled during battery cycling, we can skip the low-temperature step to directly fabricate graphene oxide. Figure 3a shows the digital photos of graphene oxide produced by the simplified, one-step Hummers method, in which graphite only reacted with the oxidizing agent for 6 h at 40 °C. The one derived from anode graphite showed better homogeneity than the one derived from pristine graphite. After centrifuging and diluting, the graphene oxide derived from pristine graphite exhibited notable aggregation while the graphene oxide from the anode graphite remained homogeneous (Figure 3b). Comparing with the anode graphite (47.4 m^2/g), the graphene oxide exhibited much higher specific surface area (297.8 m^2/g). More importantly, a hysteresis loop appeared in the absorption/desorption curve (Figure S6), indicating the existence of pores with size ranging from 2 to 10 nm. Due to the attachment of functional groups, the thickness of monolayered graphene oxide sheets is slightly larger than that of graphene, ranging from 0.7 to 0.9 nm. Figure 3c is a typical atomic force microscopy (AFM) image of a single-layered graphene oxide sheet with a thickness of 0.87 nm. Figure S7 presents the thickness distribution of graphene oxide sheets, showing that most of the them were single-layered. TEM imaging revealed that the graphene oxide flakes had thin and wrinkled morphology (Figure 3d). HRTEM inspection of the obtained graphene oxide showed no long-range crystalline order (Figure 3e), which was validated by the blurry halo in the fast Fourier transform (FFT) pattern (Figure 3f) and the weak, broad peak in the XRD spectrum (Figure S8). The lack of long-range ordered crystal structure suggested a high level of oxidation, which was proven by XPS inspection, showing a high oxygen content of 40.4% with a C/O ratio of 1.475 (Figure S9a). The C 1s peak in the XPS spectrum revealed the existence of C—(C, H) (283.5 eV), C—(O, N) (285.6 eV), and O=C—O (287.3 eV) bonds (Figure 3g).[55] The O 1s peak suggested the existence of O (C=O) (531.3 eV) bonds (Figure S9b). These results were consistent with previous studies.[35−38]

To demonstrate the advantages of graphene oxide derived from anode graphite in practical application, the graphene oxide was used in energy storage. The reduced graphene oxide flakes from anode graphite and pristine graphite were used to assemble symmetric supercapacitors. The cyclic voltammetry (CV) curve measured at 50 mV/s of the symmetric supercapacitor assembled by reduced graphene oxide derived from anode graphite exhibited a quasi-rectangular shape and larger area than that of the symmetric supercapacitor assembled by reduced graphene oxide derived from pristine graphite, indicative of an outstanding charge/discharge stability and a higher specific capacitance (Figure 3h). Galvanostatic

DOI: 10.1021/acs.nanolett.8b04410
Nano Lett. 2019, 19, 512−519

tests were carried out at a current density of 0.5 A/$g_{graphene\ oxide}$ to identify the specific capacitance via eq 1 (Figure 3i):

$$C_{sp} = 4C = \frac{4It}{(\Delta V)m} \quad (1)$$

where C_{sp} is the specific capacitance, I is the current, t is the discharge time, ΔV is the potential difference, and m is the weight of active material. The specific capacitance of the symmetric supercapacitor constructed with reduced graphene oxide derived from anode graphite was 311.7 F/g, 3.15 times higher than that of the symmetric supercapacitor with the reduced graphene oxide derived from pristine graphite (98.94 F/g). Clearly, battery cycling endows the graphene oxide from anode graphite with some distinguished advantages: battery cycling serves as a prefabrication step for producing graphene oxide flakes, shortening the graphene oxide fabrication time period, and enabling the process milder. The expanded lattice of anode graphite also resulted in higher specific surface area and better dispersing ability of the as-fabricated graphene oxide sheets, leading to more interfaces for chemical reactions and thereby enhancing electrochemical properties of the assembled symmetry supercapacitors.

Conversion of Anode Graphite into Graphene. Large, intact graphene films are useful in electronic devices while small graphene flakes often find more applications in energy storage, metal/polymer composites, and medicines.[25−31] However, the inevitable aggregation due to insufficient exfoliation and the demand for organic solutions for dispersion hindered the real-life utilization of graphene flakes. Moreover, the productivity of high-quality graphene is low; more than 80% of the graphite is wasted. Since the anode graphite is preswelled during battery charge/discharge, the productivity of graphene should be improved if anode graphite is used. To verify the assumption, 1.5 g of anode graphite was shear mixed for 4 h at room temperature in 200 mL of deionized water. A 1.5 g sample of pristine graphite was also shear mixed at the same condition as a control sample for comparison. As shown in Figure 4a, both the obtained graphene suspensions became dark black after shear mixing. After 4 h of standing, the graphene suspension derived from pristine graphite exhibited aggregation and deposition while the graphene suspension derived from anode graphite stayed dark black like before. After 48 h, the graphene suspension derived from pristine graphite separated into clean upper liquid and black powder bottom. In contrast, the suspension derived from anode graphite remained a black suspension with only minor separation. The productivity of graphene can be calculated by the weight of graphene remained in the liquid. Specifically, 5 mL of suspension was taken out from the upper liquid and dried. The graphene was weighed by a high-accuracy scale and the weight value was multiplied by 40. The graphene derived from pristine graphite was only 0.09−0.12 g after 48 h, corresponding to 6−8% graphene productivity. On the contrary, the graphene productivity of anode graphite was 33−36%, 4 times higher than that of pristine graphite. The higher graphene productivity stems from two major reasons. First, the lattice expansion induced by battery cycling weakened the bonding between graphite layers, leading to higher exfoliation efficiency; second, as proven by XPS (Figure S10), the graphene flakes derived from anode graphite were attached by functional groups containing oxygen, which may prohibit the aggregation. TEM inspection (Figure 4b) revealed that the graphene from anode graphite was thin and transparent. The graphene sheet had an intact crystal structure (Figure 4c) that was also validated by the FFT pattern (Figure 4d). Again, battery cycling that served as a prefabrication step effectively improved the efficiency of shear mixing without deteriorating the crystal structure of graphene sheets.

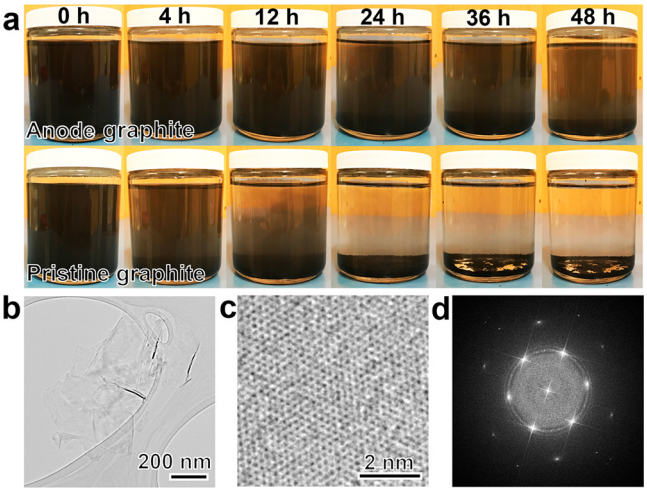

Figure 4. Graphene derived from anode graphite by shear mixing. (a) Chronological digital photos of graphene derived from anode graphite and pristine graphite. (b) TEM inspection of the graphene sheets derived from anode graphite. (c) Close-up observation of crystal structure of the graphene derived from anode graphite. (d) FFT spectrum of the graphene sheet derived from anode graphite.

Although the productivity of graphene was highly improved by using anode graphite, it is still far away from the expectation of industrial production. We need to insert the proposed strategy seamlessly into the existing cathode recycling processes with the goal of accelerating comprehensive battery recycling in a low-cost manner. Wang and co-workers[17] developed a battery recycling streamline that can readily extract lithium salts from end-of-life cathodes with a controllable proportion of Ni, Co, and Mn. In the first step of the leaching process, the shredded anode and cathode were stirred with H_2SO_4. After stirring, cathodes dissolved into the acid while anodes (graphite powders) were deposited and removed as a waste. Intriguingly, stirring with high concentration acid swells the graphite. If the anode graphite is further swelled by the acid treatment, the productivity by shear mixing is expected to be remarkably improved (Figure 5a). This provides a seamless integration of cathode recycling and graphene production, enabling a complete recycling of a Li-ion battery. To verify the assumption, 1.5 g of anode graphite powders was stirred with cathode materials ($LiCoO_2$) in 4 M H_2SO_4 solution for 4 h. $LiCoO_2$ was dissolved into the acid and graphite was deposited and rinsed by dilute water three times. The acid-treated anode graphite was thin and transparent under TEM (Figure 5b), indicating that the van der Waals bonds had been weakened so much that the ultrasonication broke the bond connections. Close-up inspection of the acid-treated anode graphite revealed irregular staking of graphene layers (Figure 5c) with a multicrystalline structure feature (Figure 5d).

After shear mixing, the graphene suspension from H_2SO_4-treated anode graphite displayed no notable separation and disposition even after 120 h (Figure 6a). The graphene from H_2SO_4-treated anode graphite remained in the liquid was 1.26

DOI: 10.1021/acs.nanolett.8b04410
Nano Lett. 2019, 19, 512−519

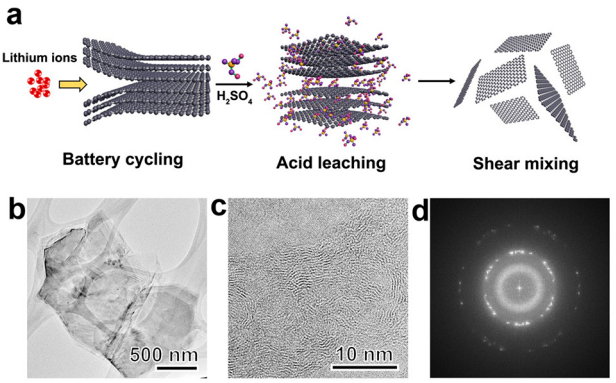

Figure 5. Acid treatment of anode graphite. (a) Schematic diagram of the graphite lattice expansion due to battery cycling and acid leaching. (b) TEM image of H_2SO_4-treated anode graphite powders. (c) HRTEM image of the acid-treated anode graphite powders. (d) FFT of Figure 5c.

g after 48 h and 0.95 g after 120 h, corresponding to 83.7% and 63.3% graphene productivity, 2 times higher than that of the untreated anode graphite and 10 times higher than that of the pristine graphite (Figure 4a). AFM inspection (Figure 6b) and the thickness distribution measured by AFM (Figure S11) imaging showed that most of the obtained graphene sheets were thin, less than seven atomic layers. The Raman spectrum at about ~2700 cm^{-1} exhibited a single, sharp, high-intensity 2D peak while the intensity ratio between the G peak at ~1580 cm^{-1} and the 2D peak was about 2, suggesting the existence of single-layered graphene with intact crystal structure (Figure 6c).[56] The specific surface area of the graphene (424.9 m^2/g) was almost 10 times higher than the anode graphite (47.4 m^2/g). However, unlike the graphene oxide, the graphene flakes did not show a hysteresis loop in the absorption/desorption curve (Figure S12) because graphene flakes were flat and flawless; thus no pores formed. Comparing with the graphene derived from untreated anode graphite (Figure S10), the acid treatment with cathode materials introduced more oxygen and a small amount of F (0.5%) and Co (0.1 wt %) to the obtained graphene sheets (Figure S13). The C 1s XPS spectrum indicated the existence of C−(O, N) bonds (285.41 eV), carbonyls (288.02 eV), and C−F bonds (291.22 eV) (Figure 6d). These functional groups further prevented the aggregation of graphene flakes. A critical question is whether the acid treatment damaged the crystal structure of the graphene. TEM inspection (Figure 6e) unveiled that the graphene from the H_2SO_4-treated anode graphite is thin and flexible. The HRTEM image (Figure 6f) and corresponding reversed FFT image (Figure 6g) showed no visible defects, indicating that the acid treatment only broke the van der Waals bonds but had little influence on the sp2 bonds due to the much lower concentration of H_2SO_4 comparing with Hummers method. This assumption was further verified by the weak but sharp (002) peak in the XRD spectrum (Figure S14), which suggests a low degree of stacking but a high degree of crystallinity.

To demonstrate the superior advantages of the anode graphene (the graphene sheets obtained from H_2SO_4-treated anode graphite) in practical application, 1 wt % of the anode graphene sheets and agglomerated graphene from pristine graphite (as a reference for comparison) were separately mixed with epoxy (EPO-TEK, 302-3M, Epoxy Technology Inc.). Three-point bending tests were carried out on the composites and epoxy specimens (five beam specimens with the dimension of 40 × 7 × 5 mm (length × width × height) were tested for each material). Figure 6h shows a graphene sheet protruded out from the anode graphene/epoxy composite fracture surface, indicating strong bonding between the anode graphene and matrix. In contrast, pure epoxy exhibited a flat fracture surface (Figure S15a) while the pristine graphite derived agglomerated graphene/epoxy composite (Figure S15b) displaced thick, agglomerated graphene particles on the fracture surface. Typical three-point bending flexural stress−strain curves of pure epoxy, anode graphene/epoxy composite, and pristine graphite derived agglomerated graphene/epoxy composite were illustrated in Figure 6i. The pristine graphite derived agglomerated graphene/epoxy composite exhibited a flexural strength of 89.8 MPa, elastic modulus of 2.5 GPa, and toughness (here referred to the area under stress−strain curve) of 1826.6 kJ/m^3, representing 7.6%, 3.8%, and 9.1% reduction compared to the pure epoxy sample (flexural strength 97.2 MPa, elastic modulus 2.6 GPa, and toughness 2008.6 kJ/m^3) (Figure 6j)). Therefore, the agglomerate graphene flakes (Figure S15b) not only had weak bonding with the matrix but also caused delamination between the flakes and matrix, acting as the source of cracks to deteriorate the composite's mechanical performance. On the contrary, the anode graphene/epoxy composite exhibited a significantly improved flexural strength (122.5 MPa), elastic modulus (3.6 GPa), and toughness (2269.9 kJ/m^3), corresponding to a 26.0%, 38.5%, and 13.0% amplification over the epoxy control sample (Figure 6j). Such superlative mechanical performance is ascribed to the advantages of graphene sheets stemming from battery cycling, which not only improved the production efficiency but also grafted functional groups onto the anode graphene sheets. The surface functional groups enabled better dispersibility and stronger bonding between the graphene and epoxy (Figure 6h). The anode graphene should find more applications in energy storage and composites.

In summary, the graphite powders collected from end-of-life Li-ion batteries exhibited irregular expansion along the crystallographic *c*-direction. MD simulations uncovered that the Li-ion intercalation and deintercalation during charge/discharge induced the lattice expansion, which inevitably damaged the van der Waals bonds and weakened the interlayer bonding strength of graphite. Since the fabrication of graphene and graphene oxide is to break the bonds and separate the graphene layers, the battery cycling can be considered as a prefabrication step, which can largely enhance the productivity of graphene and its derivatives. To verify the assumption, graphene oxide was first fabricated via the simplified Hummers method. Comparing with the graphene oxide derived from pristine graphite, the graphene oxide from anode graphite exhibited superlative homogeneity and electrochemical properties. Subsequently, graphene was fabricated by shear mixing. The lithiation aided pre-expansion enabled a 4 times enhancement of graphene productivity. Furthermore, the graphene fabrication was seamlessly inserted into the currently used battery recycling streamline in which 4 M H_2SO_4 was used to dissolve cathode materials while the insoluble anode graphite was removed. The acid treatment was found to further swell the graphite lattice without damaging the sp2 bonds, pushing up the graphene productivity to 83.7% (10 times higher than that of pristine graphite powders). The epoxy reinforced by the battery anode derived graphene exhibited a remarkable increase in mechanical properties. The findings present a new promise for smartly recycling Li-ion batteries.

DOI: 10.1021/acs.nanolett.8b04410
Nano Lett. 2019, 19, 512−519

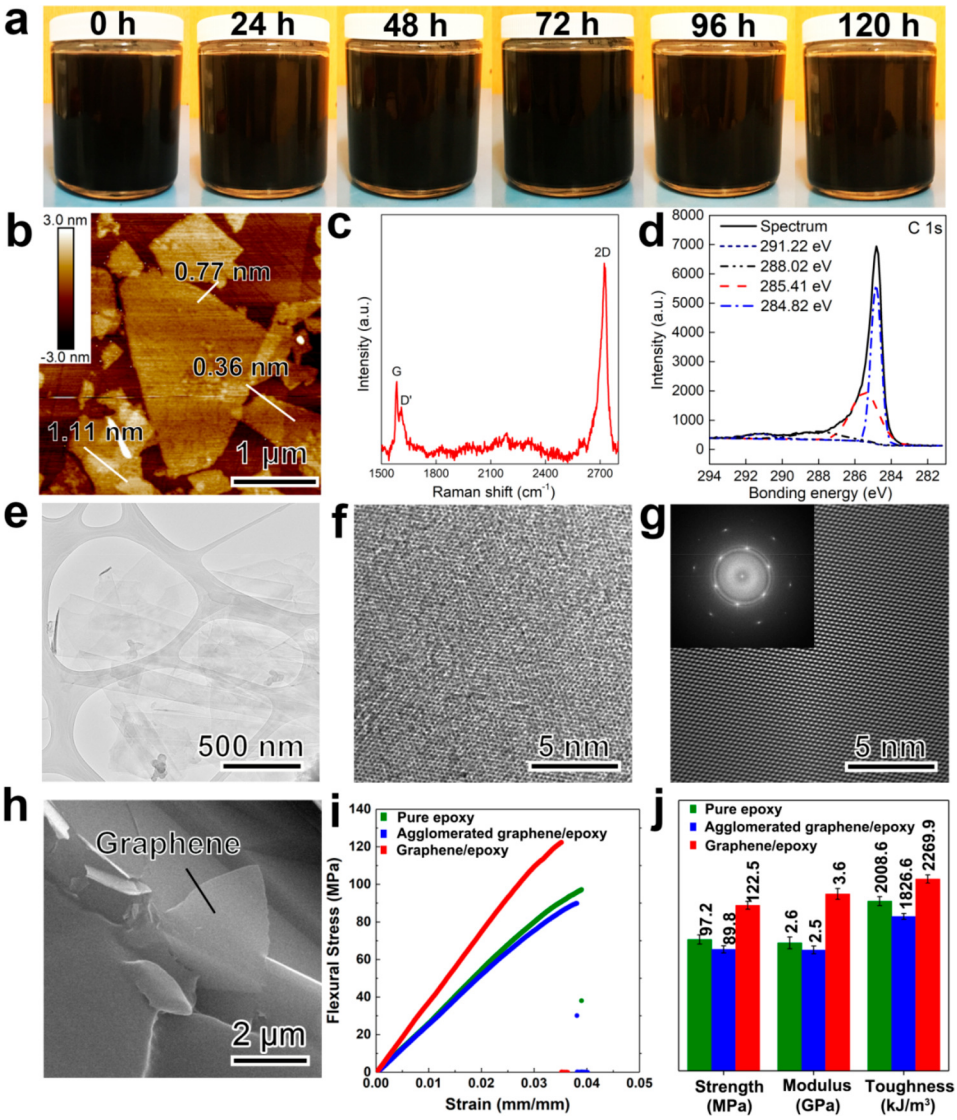

Figure 6. Fabrication of graphene from acid-treated anode graphite. (a) Chronological digital photos of graphene suspension derived from acid-treated anode graphite. (b) AFM height profile of the as-fabricated graphene flakes. (c) Raman spectrum of the as-fabricated graphene. (d) XPS C 1s spectrum of the graphene. (e) TEM image of the graphene sheets derived from acid-treated anode graphite. (f) HRTEM inspection of the graphene sheet derived from acid-treated anode graphite. (g) Convoluted lattice image of Figure 6f, showing no visible defects. (h) A graphene sheet protruded out from the anode graphene/epoxy composite fracture surface. (i) Flexural stress−strain curves of epoxy and graphene reinforced composites. (j) Comparison of flexural strength, elastic modulus, and toughness for pure epoxy and composites reinforced by agglomerated graphene derived from pristine graphite and graphene from acid-treated anode graphite.

■ ASSOCIATED CONTENT

Supporting Information

The Supporting Information is available free of charge on the ACS Publications website at DOI: 10.1021/acs.nanolett.8b04410.

Experimental details, XPS spectra of anode graphite, graphene oxide, and graphene, particle size distribution, lattice parameter, crystal structure schematic diagram, DFT calculation schematic diagram, nitrogen absorption and desorption curves of graphite, graphene oxide, and graphene, XRD spectra of anode graphite, graphene oxide, and graphene, thickness distribution of graphene oxide and graphene, SEM images of pure epoxy and pristine graphite derived agglomerated graphene/epoxy composite (PDF)

■ AUTHOR INFORMATION

Corresponding Author

*X. Li. E-mail: xl3p@virginia.edu. Tel: 434-243-7762.

ORCID

Yunya Zhang: 0000-0002-9411-0184

Ningning Song: 0000-0003-0710-2133

Author Contributions

#Contributed equally as lead authors.

Notes

The authors declare no competing financial interest.

■ ACKNOWLEDGMENTS

Financial support for this study was provided by the U.S. National Science Foundation (CMMI-1728042). The authors

DOI: 10.1021/acs.nanolett.8b04410
Nano Lett. 2019, 19, 512−519

thank the staff members at the University of Virginia NMCF for electron microscopy technical support.

REFERENCES

(1) Scrosati, B. *Electrochim. Acta* **2000**, *45*, 2461−2466.
(2) Etacheri, V.; Marom, R.; Elazari, R.; Salitra, G.; Aurbach, D. *Energy Environ. Sci.* **2011**, *4*, 3243−3262.
(3) Li, L.; Lu, J.; Ren, Y.; Zhang, X. X.; Chen, R. J.; Wu, F.; Amine, K. *J. Power Sources* **2012**, *218*, 21−27.
(4) Wang, X.; Gaustad, G.; Babbitt, C. W. *Waste Manage.* **2016**, *51*, 204−213.
(5) Li, L.; Zhang, X.; Chen, R.; Zhao, T.; Lu, J.; Wu, F.; Amine, K. *J. Power Sources* **2014**, *249*, 28−34.
(6) Choi, H.; Shin, J.; Woo, J. R. *Energy Policy* **2018**, *121*, 13−24.
(7) Lu, L.; Han, X.; Li, J.; Hua, J.; Ouyang, M. *J. Power Sources* **2013**, *226*, 272−288.
(8) Gaines, L. *SM&T* **2014**, *1*, 2−7.
(9) Wang, X.; Gaustad, G.; Babbitt, C. W.; Richa, K. *Resour. Conserv. Recy.* **2014**, *83*, 53−62.
(10) Wang, X.; Gaustad, G.; Babbitt, C. W.; Bailey, C.; Ganter, M. J.; Landi, B. J. *J. Environ. Manage.* **2014**, *135*, 126−134.
(11) Lain, M. J. *J. Power Sources* **2001**, *97*, 736−738.
(12) Dutta, D.; Kumari, A.; Panda, R.; Jha, S.; Gupta, D.; Goel, S.; Jha, M. K. *Sep. Purif. Technol.* **2018**, *200*, 327−334.
(13) Castillo, S.; Ansart, F.; Laberty-Robert, C.; Portal, J. *J. Power Sources* **2002**, *112*, 247−254.
(14) Kim, S.; Kim, J.; Kim, S.; Lee, J.; Yoon, J. *Environ. Sci: Water. Res. Technol* **2018**, *4*, 175−182.
(15) Wang, X.; Gaustad, G.; Babbitt, C. W. *Waste Manage.* **2016**, *51*, 204−213.
(16) Zou, H.; Gratz, E.; Apelian, D.; Wang, Y. *Green Chem.* **2013**, *15*, 1183−1191.
(17) Gratz, E.; Sa, Q.; Apelian, D.; Wang, Y. *J. Power Sources* **2014**, *262*, 255−262.
(18) Li, L.; Deshmane, V. G.; Paranthaman, M. P.; Bhave, R.; Moyer, B. A.; Harrison, S. *Johnson Matthey Technol. Rev.* **2018**, *62*, 161−176.
(19) Li, L.; Dunn, J. B.; Zhang, X. X.; Gaines, L.; Chen, R. J.; Wu, F.; Amine, K. *J. Power Sources* **2013**, *233*, 180−189.
(20) Li, L.; Zhai, L.; Zhang, X.; Lu, J.; Chen, R.; Wu, F.; Amine, K. *J. Power Sources* **2014**, *262*, 380−385.
(21) Dutta, D.; Kumari, A.; Panda, R.; Jha, S.; Gupta, D.; Goel, S.; Jha, M. K. *Sep. Purif. Technol.* **2018**, *200*, 327−334.
(22) Ganter, M. J.; Landi, B. J.; Babbitt, C. W.; Anctil, A.; Gaustad, G. *J. Power Sources* **2014**, *256*, 274−280.
(23) Shi, Y.; Chen, G.; Chen, Z. *Green Chem.* **2018**, *20*, 851−862.
(24) Novoselov, K. S.; Geim, A. K.; Morozov, S. V.; Jiang, D.; Zhang, Y.; Dubonos, S. V.; Grigorieva, I. V.; Firsov, A. A. *Science* **2004**, *306*, 666−669.
(25) Novoselov, K. S.; Fal'ko, V. I.; Colombo, L.; Gellert, P. R.; Schwab, M. G.; Kim, K. *Nature* **2012**, *490*, 192−200.
(26) Zhang, Y.; Gao, Z.; Song, N.; He, J.; Li, X. *Mater. Today Energy* **2018**, *9*, 319−335.
(27) Ma, T.; Liu, Z.; Wen, J.; Gao, Y.; Ren, X.; Chen, H.; Jin, C.; Ma, X. L.; Xu, N.; Cheng, H. M.; Ren, W. *Nat. Commun.* **2017**, *8*, 14486.
(28) Gao, Z.; Yang, W.; Wang, J.; Song, N.; Li, X. *Nano Energy* **2015**, *13*, 306−317.
(29) Raccichini, R.; Varzi, A.; Passerini, S.; Scrosati, B. *Nat. Mater.* **2015**, *14*, 271−279.
(30) Gao, Z.; Zhang, Y.; Song, N.; Li, X. *Electrochim. Acta* **2017**, *246*, 507−516.
(31) Zhang, Y.; Li, X. *Nano Lett.* **2017**, *17*, 6907−6915.
(32) Cabrero-Vilatela, A.; Weatherup, R. S.; Braeuninger-Weimer, P.; Caneva, S.; Hofmann, S. *Nanoscale* **2016**, *8*, 2149−2158.
(33) Losurdo, M.; Giangregorio, M. M.; Capezzuto, P.; Bruno, G. *Phys. Chem. Chem. Phys.* **2011**, *13*, 20836−20843.
(34) Wang, M.; Jang, S. K.; Jang, W. J.; Kim, M.; Park, S. Y.; Kim, S. W.; Kahng, S. J.; Choi, J. Y.; Ruoff, R. S.; Song, Y. J.; Lee, S. *Adv. Mater.* **2013**, *25*, 2746−2752.
(35) Hossain, M. Z.; Johns, J. E.; Bevan, K. H.; Karmel, H. J.; Liang, Y. T.; Yoshimoto, S.; Mukai, K.; Koitaya, T.; Yoshinobu, J.; Kawai, M.; Lear, A. M.; Kesmodel, L. L.; Tait, S. L; Hersam, M. C. *Nat. Chem.* **2012**, *4*, 305−309.
(36) Dikin, D. A.; Stankovich, S.; Zimney, E. J.; Piner, R. D.; Dommett, G. H. B.; Evmenenko, G.; Nguyen, S. T.; Ruoff, R. S. *Nature* **2007**, *448*, 457−460.
(37) Cao, N.; Zhang, Y. *J. Nanomater.* **2015**, *2015*, 168125.
(38) Chen, J.; Yao, B.; Li, C.; Shi, G. *Carbon* **2013**, *64*, 225−229.
(39) Paton, K. R.; Varrla, E.; Backes, C.; Smith, R. J.; Khan, U.; O'Neill, A.; Boland, C.; Lotya, M.; Istrate, O. M.; King, P.; Higgins, T.; et al. *Nat. Mater.* **2014**, *13*, 624−630.
(40) Dong, L.; Chen, Z.; Zhao, X.; Ma, J.; Lin, S.; Li, M.; Bao, Y.; Chu, L.; Leng, K.; Lu, H.; Loh, K. P. *Nat. Commun.* **2018**, *9*, 76.
(41) Yi, M.; Shen, Z. *J. Mater. Chem. A* **2015**, *3*, 11700−11715.
(42) Ramanathan, T.; Abdala, A. A.; Stankovich, S.; Dikin, D. A.; Herrera-Alonso, M.; Piner, R. D.; Adamson, D. H.; Schniepp, H. C.; Chen, X.; Ruoff, R. S.; Nguyen, S. T.; Aksay, I. A.; Prud'Homme, R. K.; Brinson, L. C. *Nat. Nanotechnol.* **2008**, *3*, 327−331.
(43) Castillo, S.; Ansart, F.; Laberty-Robert, C.; Portal, J. *J. Power Sources* **2002**, *112*, 247−254.
(44) Rothermel, S.; Evertz, M.; Kasnatscheew, J.; Qi, X.; Grützke, M.; Winter, M.; Nowak, S. *ChemSusChem* **2016**, *9*, 3473−3484.
(45) Zhang, J.; Li, X.; Song, D.; Miao, Y.; Song, J.; Zhang, L. *J. Power Sources* **2018**, *390*, 38−44.
(46) Guo, Y.; Li, F.; Zhu, H.; Li, G.; Huang, J.; He, W. *Waste Manage.* **2016**, *51*, 227−233.
(47) Zhang, W.; Xu, C.; He, W.; Li, G.; Huang, J. *Waste Manage. Res.* **2018**, *36*, 99−112.
(48) Hassel, O.; Mark, H. *Eur. Phys. J. A* **1924**, *25*, 317−337.
(49) Dahn, J. R. *Phys. Rev. B: Condens. Matter Mater. Phys.* **1991**, *44*, 9170.
(50) Dahn, J. R.; Fong, R.; Spoon, M. J. *Phys. Rev. B: Condens. Matter Mater. Phys.* **1990**, *42*, 6424.
(51) Wang, X. L.; An, K.; Cai, L.; Feng, Z.; Nagler, S. E.; Daniel, C.; Rhodes, K. J.; Stoica, A. D.; Skorpenske, H. D.; Liang, C.; Zhang, W.; Kim, J.; Qi, Y.; Harris, S. J. *Sci. Rep.* **2012**, *2*, 747.
(52) Qian, X.; Gu, X.; Dresselhaus, M. S.; Yang, R. *J. Phys. Chem. Lett.* **2016**, *7*, 4744−4750.
(53) Chen, X.; Tian, F.; Persson, C.; Duan, W.; Chen, N. *Sci. Rep.* **2013**, *3*, 3046.
(54) Zhu, Y.; Murali, S.; Cai, W.; Li, X.; Suk, J. W.; Potts, J. R.; Ruoff, R. S. *Adv. Mater.* **2010**, *22*, 3906−3924.
(55) Yu, L.; Tang, Q.; Zhang, Y.; Chen, R.; Liu, X.; Qiao, W.; Li, W.; Ruan, H.; Song, X. *Sci. Rep.* **2016**, *6*, 34980.
(56) Ferrari, A. C.; Meyer, J. C.; Scardaci, V.; Casiraghi, C.; Lazzeri, M.; Mauri, F.; Piscanec, S.; Jiang, D.; Novoselov, K. S.; Roth, S.; Geim, A. K. *Phys. Rev. Lett.* **2006**, *97*, 187401.

DOI: 10.1021/acs.nanolett.8b04410
Nano Lett. 2019, 19, 512−519